Bifurcation to worms in electroconvection

Urs Bisang and Guenter Ahlers
Department of Physics and Center for Nonlinear Science, University of California at Santa Barbara, Santa Barbara, California 93106
(Received 25 February 1999)

The primary bifurcation to electroconvection of the liquid crystal 4-ethyl-2-fluoro-4′-[2-(trans-4-pentylcyclohexyl)ethyl]-biphenyl (I52) with planar alignment leads to localized structures of convection rolls known as ''worms'' when the conductivity of the fluid is relatively small. Worms coexist with the conduction state. They have a unique small width in the direction perpendicular to the director and a varying, usually much greater, length parallel to the director. Previous experiments had not determined whether the bifurcation to worms is supercritical or subcritical. We estimated the voltage V_c corresponding to the stability limit of the conduction state by measuring the mean-square amplitude of the thermally induced fluctuations below onset and extrapolating to V_c. We found that worms appear already well below V_c. Thus the bifurcation is subcritical. Measurements of the lifetime of the conduction state below V_c gave information about the voltage V_s corresponding to the saddle node below which no worms form. We measured V_c and $\epsilon_s = V_s^2/V_c^2 - 1$ as a function of the conductance σ for a cell of thickness 24 μm and found for our sample that ϵ_s approaches zero from negative values near $\sigma \simeq 1.2\times 10^{-8}\ \Omega^{-1}\ \mathrm{m}^{-1}$ as σ increases. For larger σ we found the bifurcation to be supercritical. We have been unable to determine so far whether the experimentally observed transition with decreasing σ from a supercritical to a subcritical bifurcation occurs via a tricritical bifurcation, or whether the worm saddle node is disconnected from the primary supercritical bifurcation line as suggested by theory. [S1063-651X(99)06010-9]

PACS number(s): 05.45.−a, 45.70.Qj, 47.20.−k, 47.54.+r

I. INTRODUCTION

Under nonequilibrium conditions, a spatially extended system will often undergo a transition from a uniform state to a state with spatial variation which we call a ''pattern.'' Patterns are ubiquitous in nature. Pattern-forming systems that have been studied in detail theoretically and experimentally are, for example, convection in fluids, dendrictic growth of crystals from the melt or from solutions, directional solidification, chemical reactions, and ripples on the surface of a fluid or in a thin layer of a granular medium vibrated in the vertical direction. Well known fluid-dynamical systems where patterns have been studied extensively are Rayleigh-Bénard convection and Taylor-Couette flow [1]. Another example is electroconvection (EC) in nematic liquid crystals (NLC) [2]. This latter case is a paradigm for pattern formation in *anisotropic* systems. The work reported in the present paper involves EC.

NLC have an inherent orientational order, but no positional order [3]. The average direction of their molecular alignment is called the director $\hat{n}$. Many properties of NLC are anisotropic. Thus, for instance, the dielectric constant depends on the direction of the electric field relative to $\hat{n}$, having values $\epsilon_\parallel$ and $\epsilon_\perp$ parallel and perpendicular to $\hat{n}$, respectively. By confining a layer of NLC doped with ionic impurities between two properly treated glass plates, one can obtain a cell with uniform planar alignment of the director parallel to the plates. If the NLC has a negative anisotropy $\epsilon_a \equiv \epsilon_\parallel - \epsilon_\perp$ of the dielectric constant and an ac voltage of amplitude V is applied between the plates, then a transition from the spatially uniform state to a convecting state with spatial variation occurs as V is increased above a critical voltage V_c [4]. The precise value of V_c depends on the frequency f of the applied voltage and the conductivity σ of the NLC. The concentration of ionic impurities determines σ.

The experiments reported here were done using the NLC *4-ethyl-2-fluoro-4′-[2-(trans-4-pentylcyclohexyl)ethyl]-biphenyl* (I52) [5,6]. Electroconvection in I52 leads to a great variety of spatiotemporal structures [7–11]. Depending on σ, one finds stationary rolls, traveling waves, or spatiotemporal chaos at onset. A remarkable recent discovery was that localized states of traveling waves form at the onset of convection when σ is relatively small [10]. The occurrence of localized structures [12,13] is one of the phenomena unique to nonlinear systems. These so-called pulses coexist with the spatially uniform ground state. They were first found in a one-dimensional system [12,13], and in that case it was possible to understand them qualitatively [14,15] in terms of subcritical Ginzburg-Landau equations. However, for pulses in systems which are spatially extended in two dimensions [16] theoretical explanations are limited [17,18]. The discovery of localized traveling waves coexisting with the ground state in anisotropic two-dimensional EC [9,10] adds to the complexity of the phenomena. These states, known as ''worms,'' have a unique small width in one direction and a varying, usually much greater, length in the other. Figure 1 shows a snapshot of worms. Remarkably, it has been possible to gain theoretical insight into their nature by considering Ginzburg-Landau equations [19] based on the equations of motion [20] of the system. It will be interesting to see whether other recently observed localized structures in EC [21] can be understood in similar ways.

Worms were first observed as the control parameter (the square V^2 of the applied voltage V) reached a certain value; but initially they were very rare and became more abundant only as V^2 became larger. Their generation and decay as V was increased and decreased did not show any hysteresis

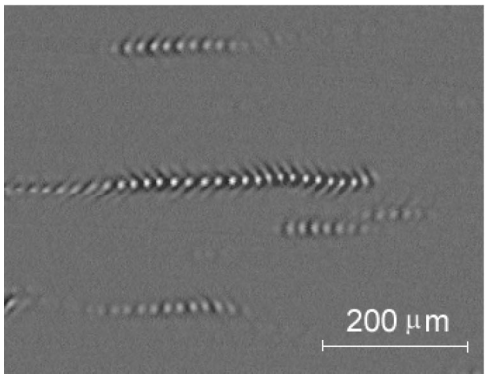

FIG. 1. Snapshot of the worm state for $\sigma = 4 \times 10^{-9}\ \Omega^{-1}\ \mathrm{m}^{-1}$ at $\epsilon = -0.17$. For this run, $d = 29\ \mu$m, $\tilde{\epsilon}_s = -0.31$, and $\tau = 934$ s. The image was taken 1600 s after the voltage was stepped up.

[9,10]. Thus it was difficult to determine directly whether the creation of worms was associated with a supercritical or a subcritical bifurcation. A recently developed Swift-Hohenberg-like [22] model equation [23] produced wormlike localized structures, but only for a strongly subcritical bifurcation. Wormlike structures were found [19] also for coupled Ginzburg-Landau equations related to the weak-electrolyte model (WEM) of electroconvection [20], in which the bifurcation to the extended state is *supercritical* [24]. But again the bifurcation to the localized state is subcritical. Recently we showed experimentally that the bifurcation to worms is indeed subcritical by measuring the critical voltage V_c [25]. The critical voltage, i.e., the bifurcation point at which the spatially uniform state became unstable to infinitesimal perturbations, was determined by measuring the mean-square amplitude $\langle \theta^2 \rangle$ of director-angle fluctuations induced by thermal-noise-driven convection-roll fluctuations [26] about the nonconvecting ground state. This amplitude is known to diverge (except for nonlinear saturation) at V_c. In a mean-field approximation, a straight line through $\langle \theta^2 \rangle^{-2}$ vs V^2 is expected to pass through zero at V_c^2 [26], thus making it possible to estimate V_c. It was found that the worms grow spontaneously out of the ground state at irreproducible locations already for applied voltages V much less than V_c, i.e., that they are indeed associated with a subcritical bifurcation. This observation suggests that the worms are nucleated in the subcritical regime by the thermal noise. This picture is supported also by measurements of the mean lifetime τ of the conduction state, which suggest a thermally activated mechanism for worm formation [25].

At higher conductivities and consistent with weakly nonlinear theory [24], a supercritical bifurcation has been found experimentally [9]. This bifurcation yielded an extended-chaos state immediately above onset. An interesting question is how the bifurcation evolves from supercritical to subcritical as σ decreases from the extended-chaos regime to the worm regime. Usually such a change occurs via a tricritical bifurcation, and the initial slopes of the mean-square amplitudes of the fields as a function of the control parameter ϵ diverge as the tricritical point is approached from the supercritical side. In this case, however, explicit calculations [24], based on the WEM, of these slopes indicate that they remain finite and thus that the bifurcation to the extended-chaos state remains supercritical. The worms then seem to be associated with a different instability not directly coupled to the first linear-instability point of the conduction state. Unfortunately our measurements are not yet detailed enough to elucidate this interesting phenomenon.

In this paper we present estimates of the critical voltage V_c, and of the value $\tilde{\epsilon}_s$ of $\epsilon \equiv V^2/V_c^2 - 1$ where worms first appear, as a function of σ. We believe that $\tilde{\epsilon}_s$ is close to the value ϵ_s where the saddle node of the subcritical bifurcation is located. Thus the measurements give information about the value of σ where the bifurcation changes from subcritical to supercritical, and about the size of the potential hysteresis loop which would exist in the absence of noise.

The remainder of this paper is structured as follows. Section II describes the experimental apparatus and techniques used for the experiment. In Sec. III we present the experimental results, and Sec. IV contains a summary and discussion of the results.

A brief report on part of this work has already appeared elsewhere [25].

II. EXPERIMENTAL METHOD

A. Experimental apparatus

The apparatus is nearly the same as the one described in Ref. [11]. It consists of a shadowgraph system with computer-controlled image acquisition, a temperature-controlled sample stage that contains the electroconvection cell, and electronics for applying the ac voltage and measuring the conductivity of the cell. The temperature-controlled sample stage is crucial for the experiment for two reasons. First, below 24 °C I52 is no longer nematic and no electroconvection can be observed [5,27]. Therefore, experiments with I52 at typical ambient temperatures are not possible. Second, the conductivity $\sigma(T)$, which depends upon the temperature T, is an important control parameter and determines the pattern-formation phenomena which are observed.

There are two main differences between the present apparatus and the one described in Ref. [11]. The first is that the sample stage is cooled by ambient air instead of being water cooled. This simplifies the operation of the experiment and makes changing cells easier and faster, but obviously only temperatures sufficiently above ambient can be used. The temperature stability of the air-cooled sample stage is ± 1 mK, about the same as that of the water-cooled stage. With air cooling, temperatures up to 200° C were accessible, although our temperatures ranged only from 29 °C to 80 ° C.

The second and more important difference is that the shadowgraph was optimized for high sensitivity, which was needed for measurements of the very weak thermal fluctuations. High sensitivity was achieved by careful positioning and aligning of the optical components, and by using a much stronger white-light source instead of the much weaker laser diode. The stronger light source made it possible to operate the charge-coupled device (CCD) camera at the level of light intensity where the camera is most sensitive to relative intensity changes, improving overall resolution considerably.

The electroconvection cells consisted of two glass plates separated by Mylar spacers and sealed by epoxy. The glass plates were coated on the inside with indium tin oxide (ITO), a transparent conductor. The coatings were used as elec-

TABLE I. Parameters for the runs. Cells 1, 2, and 3 had spacings $d=24$, 26, and 29 μm, respectively.

Cell	$10^8\sigma$ (Ω^{-1} m^{-1})	$-\tilde{\epsilon}_s$	V_c (V)	V_s (V)	T(°C)
1	0.37	0.592	25.70	16.40	32.75
1	0.50	0.481	19.30	13.90	55.10
1	0.65	0.378	16.97	13.38	60.00
1	0.82	0.230	14.37	12.61	65.00
1	0.94	0.178	14.45	13.10	70.50
1	1.02	0.116	13.89	13.06	77
2	1.31		10.18		64.50
3	0.40	0.31	20.76	17.3	38.00

trodes to apply a voltage across the cell. The three main cells and the parameters of the runs for which they were used are listed in Table I. For the determination of the onset of convection we used cells 1 and 2 of thicknesses $d=24\pm1$ and 26 ± 1 μm. Cell 3, with $d=29$ μm, was used to obtain illustrative images of worms in the subcritical regime. Many of the conductivity measurements were made in additional cells with d between 24 and 50 μm. The cells were uniform to about ±0.5 μm and the sample area was roughly 0.5 cm $\times$ 0.5 cm. Planar alignment of the liquid crystal was obtained by using rubbed polyimide films which were spin coated onto the glass plates. The electronic circuit described in Refs. [11,27] was used to measure the resistance R of the cells. The conductivity $\sigma=(d/A)\times1/R$ of a cell can then be calculated. Here A is the area of the electrodes. The accuracy of σ was approximately 5% and was limited by uncertainties in A and d. For a given cell, A and d were constant and thus changes in the conductivity could be measured with a precision of a few tenths of a percent. Only the component of the conductivity perpendicular to the director was determined. It turns out that σ depends on the frequency and also slightly on the applied voltage. Further information about properties of σ and its frequency dependence can be found in Ref. [27]. For the results reported here σ was measured at 50 Hz and at a voltage of 2.7 V, except when we studied the frequency or voltage dependence of σ itself.

The I52 had to be doped with 2–5 % by weight of molecular iodine (I_2) in order to get a large enough σ to achieve electroconvection [11]. Below a certain conductivity σ_{cf} no overturning electroconvection occurred, and only so-called dielectric convection [2] could be observed at relatively high voltages. The value of σ_{cf} depended sensitively on d. For thick cells σ_{cf} was smaller than for thin ones. For cell 1 with $d=24$ μm we found $\sigma_{cf}=3\times10^{-9}$ Ω^{-1} m^{-1}.

The precise value of σ could be varied by changing the temperature. Over the temperature range used in our experiments σ could be changed easily by a factor of 3–4. Unfortunately, σ decreased slowly over time, typically at a rate of 1.5×10^{-11} Ω^{-1}m^{-1}day^{-1}, because the ionic impurities tended to recombine and segregate as I_2 at the cell edges. We compensated for the decrease in σ by slowly increasing the temperature, making σ constant within ±2% over the duration of several months of the entire investigation. However, the useful lifetime of a given cell was limited to about one year.

B. Doping

Usually, we added 2–5 % by weight I_2 to pure I52 and cured the mixture for three to four weeks at 50 °C. It is important to wait that long to give the Iodine enough time to dissolve, dissociate, and interact with the I52. The temperature of 50 °C was chosen because it is similar to that of most of our experiments. Because of color changes of the sample during the curing process and while filling the cells we believe that the I_2 concentration actually decreased significantly over time. Thus we do not know the final I_2 concentration in the convection cells. However, I52 prepared this way had a sufficiently high conductivity for most of our measurements.

Recently, we experimented with *highly* doped I52 in an attempt to get EC cells with *very* high conductivities. We tested cells with $25\lesssim d\lesssim50$ μm and I52 doped with 10–25 % I_2, and found that they behaved very differently from the cells with the usual doping. Previously it was believed that the exact amount of dopant is not critical, and that above a certain concentration of I_2 the solution just saturates and the rest of the iodine does not get dissolved. Therefore the highly doped cells should have behaved essentially the same as the 2–5 % doped cells. However, they showed time-independent patterns of convection rolls at onset over the whole accessible conductivity range 3×10^{-9}–3×10^{-8} Ω^{-1} m^{-1}, instead of a Hopf bifurcation to worms or STC as observed with lesser doping. These static patterns looked very similar to the ''static oblique'' patterns SO1 and SO2 usually observed above a *secondary* bifurcation from the STC state [11] at higher values of ϵ. At sufficiently high ϵ the static patterns became unstable. A time-dependent state occurred which, with further increase of ϵ, evolved into a turbulent state at very high ϵ. This behavior above secondary bifurcations is not unlike what is usually observed also for smaller doping.

III. RESULTS

A. Thermal fluctuations

As mentioned in Sec. I, the critical voltage V_c (the limit of stability to infinitesimal perturbations) of the spatially uniform perfect-conduction state can be estimated by measuring the mean-square amplitudes of thermally (k_BT) induced fluctuations [25]. We used this method and cell 1 to determine V_c as a function of σ. For these measurements the frequency of the applied voltage was 25 Hz.

The fluctuations and convection patterns were imaged using the shadowgraph technique [11,28]. An eight-bit gray-scale frame grabber was used to digitize the images. Since the fluctuations are very weak, a series of 256 images $\tilde{I}_i(\mathbf{x},\epsilon)$ was taken at each value of ϵ. The time between images was typically 5 s, and successive images were essentially uncorrelated. There is an additional complication if the onset measurement is performed at low conductivities where worms are observed. Since the bifurcation to worms is subcritical, worms form already below onset and, by virtue of their overwhelmingly large amplitudes, interfere with the fluctuation measurements [25]. Therefore images had to be taken before worms formed. However, close to onset worms formed very quickly, and for $\epsilon\gtrsim-0.08$, it was impossible to accumulate

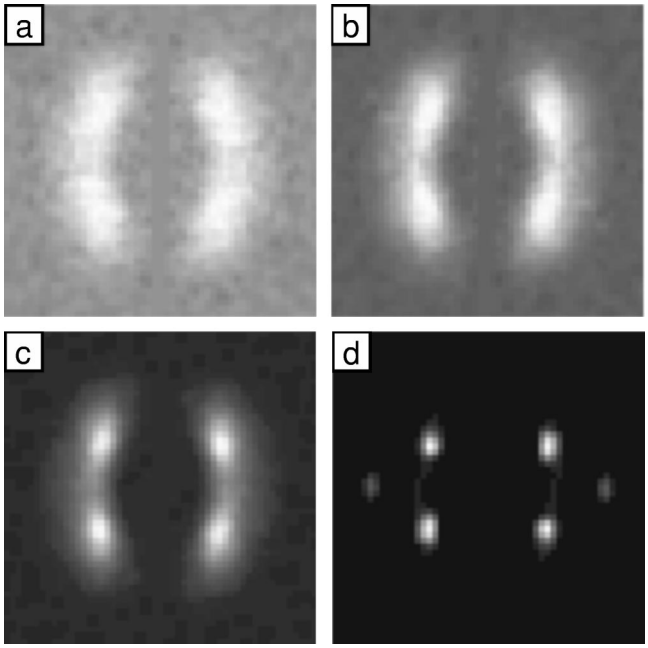

FIG. 2. Time-averaged structure factors $S(\mathbf{k})$ of the fluctuations for (a) $\epsilon=-0.270$, (b) $\epsilon=-0.093$, (c) $\epsilon=-0.016$, and (d) $\epsilon=-0.005$. The four peaks correspond to the zig and zag modes which are seen also in the extended-chaos state above onset ($\epsilon>0$). The director is in the horizontal direction. The conductivity is $\sigma=1.31\times10^{-8}\ \Omega^{-1}\ \mathrm{m}^{-1}$ and $d=26\ \mu$m. For this case the bifurcation is supercritical.

enough images in their absence when σ was small. Close to the extended-chaos region where the bifurcation is supercritical or only weakly subcritical we do not have this problem and measurements closer to onset are possible.

For each image the signal

$$I_i(\mathbf{x},\epsilon)\equiv[\tilde{I}_i(\mathbf{x},\epsilon)-\tilde{I}_0(\mathbf{x},\epsilon)]/\tilde{I}_0(\mathbf{x},\epsilon) \tag{1}$$

was calculated. Here $\tilde{I}_0(\mathbf{x},\epsilon)$ is a background image obtained by averaging all 256 images. For each $I_i(\mathbf{x},\epsilon)$ the structure factor (the square of the modulus of the Fourier transform) $S_i(\mathbf{k},\epsilon)$ was calculated and the 256 $S_i(\mathbf{k},\epsilon)$ were averaged to get $S(\mathbf{k},\epsilon)$ [29].

Figure 2 shows four examples of $S(\mathbf{k},\epsilon)$ for different values of ϵ measured for cell 2 ($d=26\pm1\,\mu$m) below onset at a conductivity of $\sigma=1.31\times10^{-8}\ \Omega^{-1}\ \mathrm{m}^{-1}$. The sample had been doped with 5% I_2. For these parameter values we expect the bifurcation to be supercritical and to the extended-chaos state rather than to worms. There are four peaks corresponding to two sets of rolls oriented obliquely to $\hat{n}$. These two modes are known as zig and zag modes and are also seen in the extended-chaos state above onset [11]. The features of $S(\mathbf{k},\epsilon)$ shown here are also very similar to those seen below onset at small conductivities in the worm regime as shown in Ref. [25]. The examples in Fig. 2 show that the peaks of $S(\mathbf{k},\epsilon)$ get sharper as one gets closer to onset, as expected from theory [30]. They also get larger, but since the gray levels of each example in Fig. 2 are scaled separately, this is not immediately apparent.

In order to get the mean-square amplitude $\langle A^2\rangle$ of the signal fluctuations from the structure factor, one has to integrate over the peaks of $S(\mathbf{k},\epsilon)$ in $\mathbf{k}$ space. This integral corresponds to $\langle A^2\rangle$. Since the fluctuating pattern is very weak, the background due to instrumental noise is significant. In principle it would be possible to do two-dimensional fitting of $S(\mathbf{k})$, but it is simpler and more reliable to calculate first the azimuthal average $S(k)$ from the data and then do one-dimensional fitting. Four examples of $S(k)$ for different ϵ values are shown in Fig. 3. We fitted a suitable function

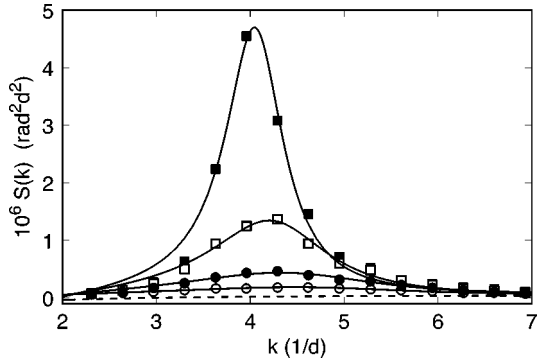

FIG. 3. The azimuthally averaged structure factor $S(k)$ as a function of the modulus k of $\mathbf{k}$ for $\epsilon=-0.005$ (closed squares), $\epsilon=-0.016$ (open squares), $\epsilon=-0.093$ (closed circles), and $\epsilon=-0.270$ (open circles). The conductivity is $\sigma=1.31\times10^{-8}\ \Omega^{-1}\ \mathrm{m}^{-1}$ and $d=26\ \mu$m. The solid lines are the fits to the data, and the dashed line is the background obtained from the fits as described in the text.

$$S(k)=[P(k)+B(k)]/2\pi k \tag{2}$$

to the azimuthally averaged structure factors. These fits are shown as solid lines in Fig. 3. In Eq. (2), $P(k)$ is the contribution of interest from the peak and $B(k)$ is the smooth background due to instrumental noise. A Lorentzian

$$P(k)=\frac{S_0}{(k-k_0)^2+\Gamma^2} \tag{3}$$

was used for the peak. The background is given by the dashed line. It was much larger at small and large k beyond the range of Fig. 3. Thus it contributed overwhelmingly to the variance (total power) of the images even though it constituted only a modest correction in the k range of interest here. A polynomial in k plus a term proportional to $1/k$ was used for $B(k)$. It did not change significantly from one ϵ value to another. Empirically, we found that the $1/k$ term had to be included to account for the rapid increase of $S(k)$ near $k=0$ (this increase is masked out in the examples in Fig. 2 in order to permit gray scales which make the fluctuations visible). After the fit of Eq. (2) to the data, the mean-square amplitude $\langle A^2\rangle$ was obtained from

$$\langle A^2\rangle=\int_0^\infty P(k)dk=\frac{S_0}{\Gamma}\left[\frac{\pi}{2}+\arctan\left(\frac{k_0}{\Gamma}\right)\right]. \tag{4}$$

For a comparison with theoretical results, $\langle A^2\rangle$ had to be converted to the mean-square amplitudes $\langle\theta^2\rangle$ of the director-angle fluctuations. For our experimental setup $\langle A^2\rangle$ and $\langle\theta^2\rangle$ are related by [28]

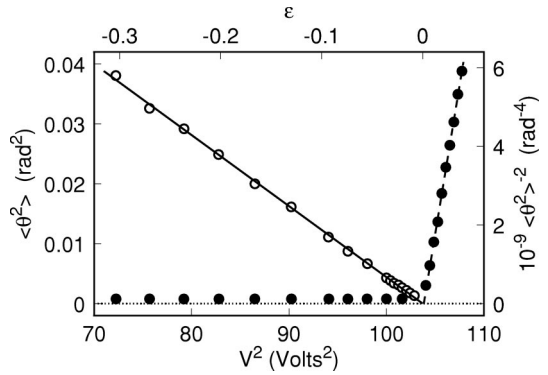

FIG. 4. The inverse square of the mean-square director-angle fluctuations $\langle\theta^2\rangle^{-2}$ (open circles, right ordinate scale) as a function of the applied voltage squared V^2 for $\sigma=1.31\times10^{-8}\ \Omega^{-1}\ \mathrm{m}^{-1}$ and $d=26\ \mu$m. The solid straight line is a fit to the data. Its intercept with the horizontal axis gives $V_c^2=103.72$. The solid circles are the variance $\langle\theta^2\rangle$ vs V^2 (left ordinate scale) and the linear extrapolation from above onset (dashed line) gives $V_c^2=103.83$.

$$\langle\theta^2\rangle=\left[\frac{(1+\tilde{n})\lambda}{4\tilde{n}d}\right]^2\langle A^2\rangle. \tag{5}$$

Here $\tilde{n}=1-(n_e/n_0)^2$ with $n_e=1.6533$ and $n_0=1.5054$ the index of refraction parallel and perpendicular to the director and λ/d is the scaled wavelength of the pattern (λ/d ranged from about 1.3 in the worm regime to about 1.5 in the extended-chaos regime).

Figure 4 shows $\langle\theta^2\rangle^{-2}$ as a function of the square of the voltage V^2 (open circles) for $\sigma=1.31\times10^{-8}\ \Omega^{-1}\ \mathrm{m}^{-1}$. As expected [26], the data fall on a straight line. A fit of a straight line to the data gives $V_c^2=103.72\ \mathrm{V}^2$ or $V_c=10.184$ V. This value is used to compute ϵ and the ϵ scale shown along the top axis in Fig. 4. A straight line through the data corresponds to the theoretically expected dependence $\langle\theta^2\rangle=\theta_0^2\epsilon^{-1/2}$, and the slope of the straight-line fit gives $\theta_0=2.7$ mrad. An approximate theoretical estimate for θ_0 is given by [26]

$$\langle\theta_0^2\rangle=\frac{k_bT}{\bar{k}_{\mathrm{el}}d}, \tag{6}$$

where k_b is Boltzmann's constant and $\bar{k}_{\mathrm{el}}\simeq20.7\times10^{-12}N$ is an average orientational elastic constant of I52 [11]. This gives $\theta_0\simeq2.9$ mrad, which is in good agreement with the experimental result. Thus it appears that the observed fluctuations are of thermal origin.

When the bifurcation is supercritical, the bifurcation point can also be determined by linear extrapolation of $\langle\theta^2\rangle$ above V_c^2 back to V_c^2 where (except for fluctuation effects) $\langle\theta^2\rangle$ should vanish continuously and without hysteresis. This method was used previously in Ref. [9]. Thus, in Fig. 4 we show as solid circles $\langle\theta^2\rangle$ extracted from the same images which were used to obtain the open circles by Fourier analysis, but in this case the entire variance of the images in real space (without the elimination of experimental noise) was calculated and converted to $\langle\theta^2\rangle$ using Eq. (5). This method is much less sensitive than fitting the peaks of $S(k)$ in Fourier space, and it is impossible to measure the fluctuations

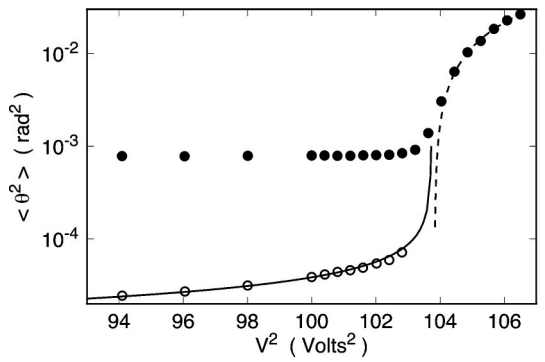

FIG. 5. The variance $\langle\theta^2\rangle$ vs V^2 of the images as a function of ϵ for the same run as in Fig. 4, but on a logarithmic vertical scale. The solid circles are obtained directly from the images, and the open ones are the power under the peak in Fourier space after background subtraction. The solid (dashed) line is the straight line in Fig. 4 which passes through the open (solid) circles.

below onset this way because they are overpowered by the experimental background noise. Above onset $\langle\theta^2\rangle$ grows steeply and the data points fall on a straight line as expected for a supercritical bifurcation. As can be seen from the figure, the intercept of a straight-line fit to the data above onset is in agreement with the value for V_c obtained from the fluctuation data below onset.

In Fig. 5 we illustrate once more the relationship between the values obtained for $\langle\theta^2\rangle$ by the two different methods. Here $\langle\theta^2\rangle$ is shown on a logarithmic scale as a function of ϵ, with the origin of the ϵ scale based on the extrapolation of the fluctuation measurements below V_c. As expected, one sees the ϵ dependence for the fluctuation measurements below $\epsilon=0$. The solid line through those data corresponds to the straight line through the open circles in Fig. 4. The solid circles are based on the variance of the images in real space. Below onset they are essentially constant and are dominated by the ϵ-independent experimental noise. Near onset these data begin to grow significantly near the ϵ value where the extrapolation of the fluctuations (solid line) seemingly diverges.

The agreement within our resolution between the values of V_c determined by the two methods in the supercritical σ range confirms that the fluctuation method below V_c can be used to determine V_c. This is important because in the worm regime, where the bifurcation is subcritical, only the fluctuation method can be used.

The inverse $1/\Gamma$ of the width of $P(k)$ is equal to an azimuthal average of the two-point correlation length ξ. The dependence of ξ on ϵ is expected to be $\xi=\xi_0(-\epsilon)^{-1/2}$. Figure 6 shows $1/\xi^2$ vs ϵ. For ϵ close to zero the data fall on a straight line, confirming the expected ϵ dependence (over a wider ϵ range a slight curvature is noticeable). A fit of the data with $\epsilon>-0.05$ to a straight line extrapolates to zero at $\epsilon=0.002$, which is quite close to the bifurcation points determined by the other two methods. The fit yields an amplitude ξ_0 equal to 0.30, which is nearly the same as the value $\xi_0=0.31$ found previously [25] in the worm regime at $\sigma=3.7\times10^{-9}\ \Omega^{-1}\ \mathrm{m}^{-1}$ and for $d=24\ \mu$m (cell 1).

We saw that $\xi(\epsilon)$ has the expected theoretical dependence on ϵ. Within error it gives the same bifurcation point as the fluctuation method and the amplitude extrapolation from

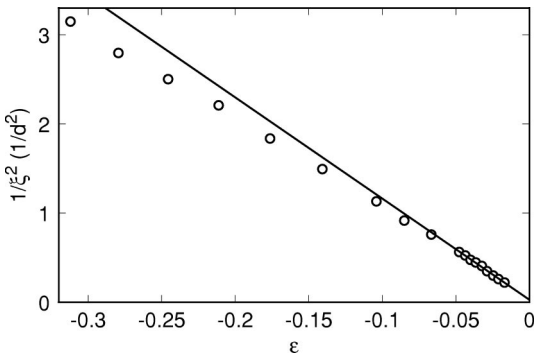

FIG. 6. The inverse square $1/\xi^2$ of the average two-point correlation length derived from the widths of $S(k)$ data like those in Fig. 3. The straight line is a fit to the data for $\epsilon > -0.05$. It passes through $1/\xi^2 = 0$ at $\epsilon = 0.0024$.

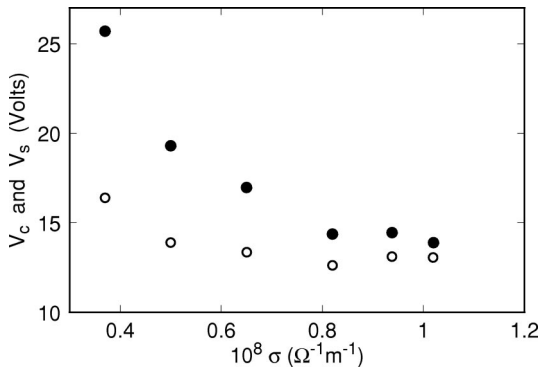

FIG. 7. Solid circles: The critical voltage V_c obtained from the fluctuation measurements as a function of σ for $d = 24$ μm. Open circles: The ''saddle-node'' point determined from the lifetime of the conduction state.

above onset. The good agreement between the three methods lends further support to the reliability of the determinations of V_c.

B. Subcriticality of the bifurcation to worms

At high conductivities we have a supercritical bifurcation to the extended-chaos state, as shown in the preceding section. An interesting question is how the bifurcation to worms, which occurs at low conductivities, evolves from subcritical to supercritical as σ increases. In order to shed some light on this issue, we made measurements of the mean lifetime τ of the conduction state below onset as a function of V for several values of σ in cell 1. The parameters of the runs are listed in Table I. A voltage $V < V_c$ was applied and then the time was measured until the first worm appeared. This measurement was performed many times at given V to get the mean lifetime $\tau(V)$. A simple algorithm was used to determine the time when the first worm had formed. A time series of images was taken at intervals of 2 s and the variance of each image was calculated in real time. When the variance had grown by a specified factor $\mathcal{F}$ from its initial value, we assumed that a worm had formed and the time since the voltage had been applied was taken to be the lifetime of the conduction state. We used $\mathcal{F} = 1.05$, but the method showed little dependence on $\mathcal{F}$. At the end of each measurement sequence an image was saved in order to verify later that a worm had actually been nucleated and that the algorithm was triggering at the right moment. The algorithm worked surprisingly well, with a 98–99 % success rate. Typically there was only one worm in the image, but sometimes two or three worms formed at roughly the same moment and in different spatial locations.

At low voltages the lifetime of the conduction state became very long, and at a low enough voltage no worms appeared during the duration of an experimental run. Since the duration of an experiment is finite, we introduced a somewhat arbitrary upper time limit of 2.5×10^4 s (about 7 h). If no worms appeared after this time, then the lifetime was considered ''infinite'' and the next measurement was started.

It was important to wait long enough between successive measurements. When the voltage was switched off and then on again too soon, worms appeared quickly and at the same spatial locations as in the previous run. We found that we had to wait at least 30 min at zero voltage between measurements to get history-independent data. We have no experimental information about the origin of this ''memory effect,'' but it seems likely that it involves slow diffusion of the ionic species in the sample. In the measurements of τ we used a waiting time of 2500 s. This long waiting time and the sometimes long lifetimes, depending on the applied voltage, made this whole experiment very time consuming. One run for a given σ took three weeks on average and the whole data taking lasted for more than four months.

In order to see the dependence of τ on ϵ, we had to determine V_c for each conductivity at which τ was measured. This was done by the fluctuation method explained in the preceding subsection and in Ref. [25]. Figure 7 shows the results for V_c as a function of σ as solid circles. For σ near σ_{cf} V_c is rather high (around 25 V). It decreases as σ increases. At high conductivities V_c becomes nearly constant at a value around 14 V. This is in agreement with the fact that at even higher conductives in the extended-chaos regime usually an onset voltage between 10 and 14 V is found, depending on the cell.

From the slopes of the straight-line fits to the fluctuation data it is possible to extract θ_0. We find that all θ_0 values are more or less the same with an average of 3.2 ± 0.5 mrad. This again is in good agreement with the theoretical value $\theta_0 = 2.9$ mrad presented in Sec. III A. Thus it appears that the worms are nucleated by thermally driven fluctuations.

Figure 8 shows τ vs ϵ for several σ. The lifetime increases with decreasing ϵ and becomes infinite below a certain value ϵ_s. We assume that this value corresponds to the saddle node of the subcritical bifurcation, below which there are no wormlike solutions. Experimentally it is difficult to measure ϵ_s directly because of the long time intervals required for it. Thus we define $\tilde{\epsilon}_s$ as the ϵ value where τ reaches an arbitrarily chosen finite value which is very large compared to the other time scales of the system. We chose this cutoff time as 10^4 s. This time is very long, but still well below the upper limit of 2.5×10^4 s for the duration of the experimental runs. An empirical exponential function was fitted to the data for $\tau(\epsilon)$. We defined $\tilde{\epsilon}_s$ as the intersection between this function and the line $\tau = 10^4$ s as shown in Fig. 8. The value of $\tilde{\epsilon}_s$ presumably is systematically larger than

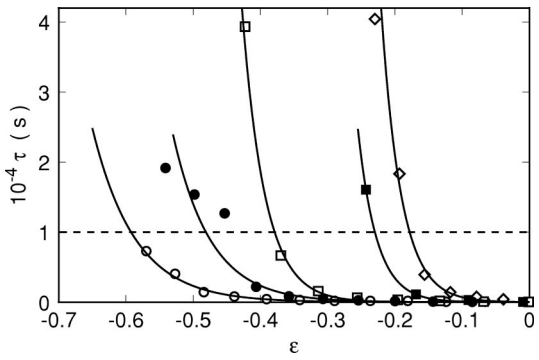

FIG. 8. Averaged mean lifetime τ of the conduction state vs ϵ for $\sigma=3.7\times10^{-9}$ Ω^{-1} m^{-1} (open circles), $\sigma=5.0\times10^{-9}$ Ω^{-1} m^{-1} (closed circles), $\sigma=6.5\times10^{-9}$ Ω^{-1} m^{-1} (open squares), $\sigma=8.2\times10^{-9}$ Ω^{-1} m^{-1} (closed squares), and $\sigma=9.38\times10^{-9}$ Ω^{-1} m^{-1} (diamonds). The cell thickness was $d=24$ μm. Exponential functions were fitted to the data and $\tilde{\epsilon}_s$ was determined by finding the intersections of these functions and the line $\tau=10^4$ s as shown in the plot.

the corresponding ϵ_s, although we believe only by a few percent. It should be a good measure for the subcriticality of the bifurcation.

The voltages V_s corresponding to $\tilde{\epsilon}_s$ for cell 1 are shown in Fig. 7 as open circles. One sees that V_s and V_c approach each other as σ increases and either merge or cross near $\sigma=1.2\times10^{-8}$ Ω^{-1} m^{-1}. This is illustrated in greater detail in Fig. 9(a), which shows $\tilde{\epsilon}_s$ vs σ. One sees that $\tilde{\epsilon}_s$ increases

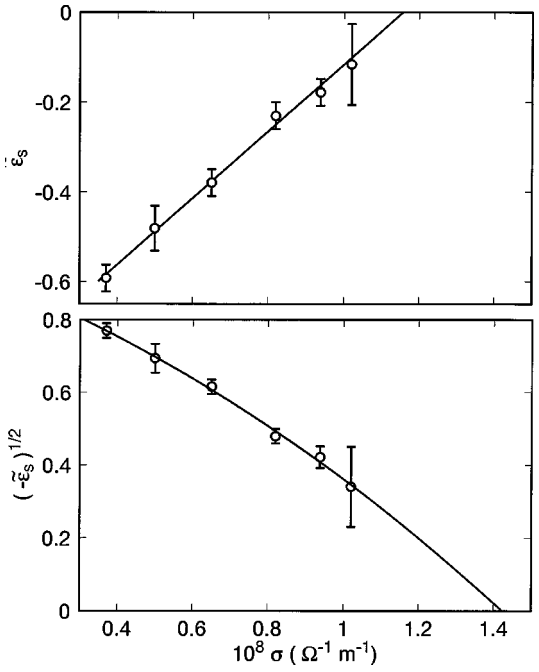

FIG. 9. The extent of the subcriticality. (a) shows $\tilde{\epsilon}_s$ as a function of the conductivity σ. The straight line is a fit to the data. Its intercept with the horizontal axis gives $\sigma_c=1.15\times10^{-8}$ Ω^{-1} m^{-1} as an estimate of the point where the observed primary bifurcation becomes supercritical. (b) shows $(-\tilde{\epsilon}_s)^{1/2}$ as a function of σ. The line is a fit of a quadratic equation to the data. It suggests $\sigma_c=1.42\times10^{-8}$ Ω^{-1} m^{-1} as the possible location of a tricritical bifurcation.

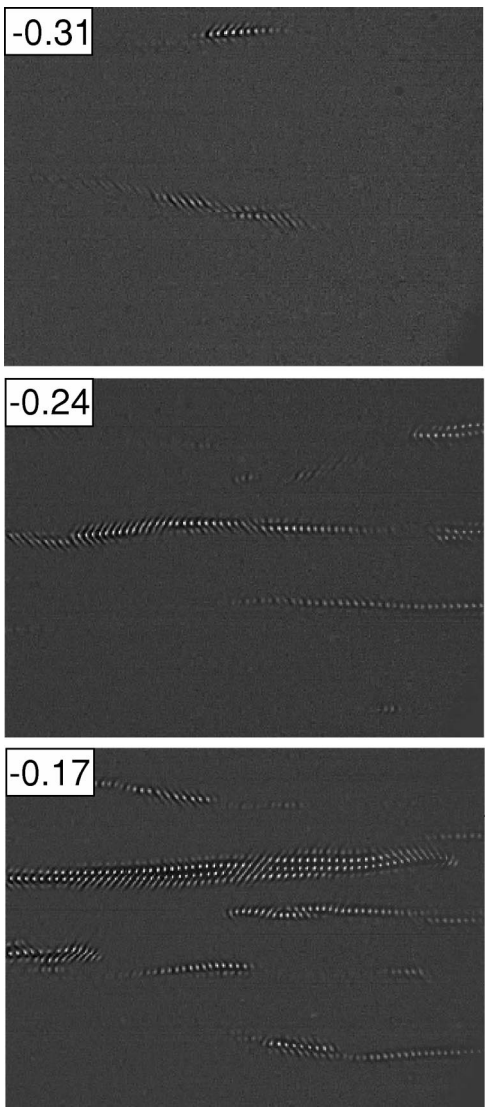

FIG. 10. Examples of worms below onset for $\sigma=0.40\times10^{-8}$ Ω^{-1} m^{-1} in a cell with $d=29$ μm. Each image covers an area of 1.24×0.93 mm. The values of ϵ are given in the figure. The director is in the horizontal direction.

with increasing σ and approaches zero from below. The data are consistent with a straight line, as shown in the figure. This line suggests that $\tilde{\epsilon}_s$ becomes 0 at $\sigma_c=1.15(\pm0.1)\times10^{-8}$ Ω^{-1} m^{-1}. For $\sigma>\sigma_c$ one observes a supercritical bifurcation to extended chaos. This interpretation implies that the saddle-node line of the subcritical bifurcation to worms simply crosses the supercritical bifurcation line to extended chaos and that there is no particular connection between these two lines. This interpretation is indeed consistent with recent theoretical predictions [24] which show that the primary bifurcation should be supercritical over the entire σ range of our experiment. In the absence of noise the worms would then bifurcate subcritically well above V_c if the extended chaos did not intervene for $V>V_c$. A remarkable aspect of this system is that the nonlinear branch of the subcritical worm bifurcation can be reached from the conduction state over a wide negative ϵ range simply due to the perturbing influence of thermally driven fluctuations.

An interpretation alternate to the one given above would involve a tricritical bifurcation [31,32] at the value of σ

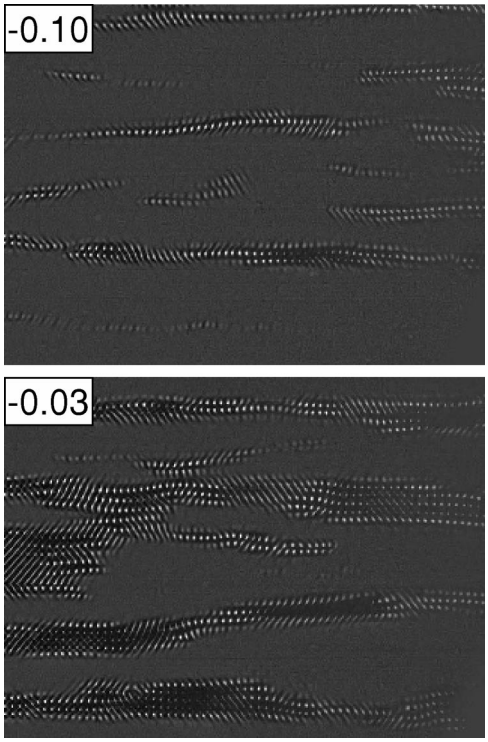

FIG. 11. Examples of worms below onset for $\sigma=0.40\times10^{-8}\ \Omega^{-1}\ \mathrm{m}^{-1}$ in a cell with $d=29\ \mu$m. Each image covers an area of 1.24×0.93 mm. The values of ϵ are given in the figure. The director is in the horizontal direction.

where the bifurcation changes from supercritical to subcritical. For a potential system without spatial extent this can be described in terms of a Landau free energy

$$F=-\frac{1}{2}\epsilon A^2+\frac{1}{4}gA^4+\frac{1}{6}kA^6, \tag{7}$$

with [to lowest order in $(\sigma_c-\sigma)$]

$$g=g_0(\sigma-\sigma_c) \tag{8}$$

and g_0 and k positive constants. For $\sigma<\sigma_c$ Eqs. (7) and (8) lead to a saddle-node line given by

$$\sqrt{-\epsilon_s}=\frac{1}{2}\frac{g_0}{\sqrt{k}}(\sigma_c-\sigma). \tag{9}$$

Thus, in Fig. 9(b) we plot $\sqrt{-\tilde{\epsilon}_s}$ as a function of σ. An excellent fit to the data in this representation is given by the solid line, which corresponds to an equation of the form $\sqrt{-\tilde{\epsilon}_s}=a(\sigma_c-\sigma)+b(\sigma_c-\sigma)^2$. Near σ_c this is consistent with Eq. (9). It yields $\sigma_c=1.42\times10^{-8}\ \Omega^{-1}\ \mathrm{m}^{-1}$, which is slightly larger than the value based on Fig. 9(a). We conclude that the tricritical interpretation is also consistent with the data, and that more detailed measurements will be required to distinguish between the two interpretations.

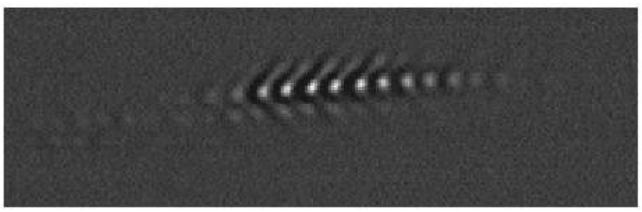

FIG. 12. Detailed image of the worm in the upper center of Fig. 10 at $\epsilon=-0.31$. This worm consists of right-traveling waves which enter the envelope on the left and leave it on the right. The director is in the horizontal direction.

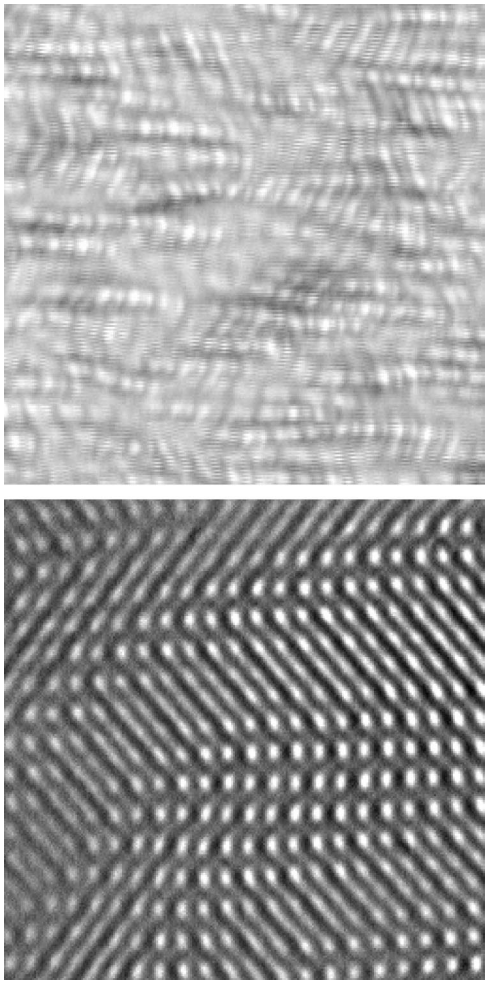

FIG. 13. Typical patterns above V_c. The top is for $\sigma=0.375\times10^{-8}\ \Omega^{-1}\ \mathrm{m}^{-1}$ and $\epsilon=0.008$ in a cell with $d=24\ \mu$m and covers an area of 0.492×0.492 mm. The bottom is for $\sigma=1.31\times10^{-8}\ \Omega^{-1}\ \mathrm{m}^{-1}$ and $\epsilon=0.009$ in a cell with $d=26\ \mu$m and covers an area of 0.497×0.497 mm. The director is in the horizontal direction.

Finally, we call attention to the fact that the exact value of σ_c depends on the cell thickness. The measurements reported here were done using cell 1 with $d=24\ \mu$m. For thicker (thinner) cells σ_c is expected to be smaller (larger).

C. Convection patterns

In Figs. 10 and 11 we show images of worms at several values of ϵ obtained with cell 3 ($d=29\ \mu$m) for $\sigma=0.4\times10^{-8}\ \Omega^{-1}\ \mathrm{m}^{-1}$. For these parameters we found $\tilde{\epsilon}_s=-0.31$. As was noted before [10,11], at voltages only very slightly above the saddle-node voltage V_s the worms are rare and most of the sample is still in the conduction state. As ϵ increases, the worms become more abundant, and near ϵ

$=0$ they fill a large fraction of the cell. With increasing ϵ the nature of the worms also seems to change somewhat in that their appearance evolves from that of a single strand of cells to structures with a greater and more irregular structure in the direction perpendicular to the director. The worms shown here have a somewhat different appearance from those in Ref. [10]. However, we believe that their precise appearance may be influenced by nonlinear optical effects which may depend on the particular setting of the shadowgraph apparatus.

In Fig. 12 we show an enlargement of the worm in the top center of Fig. 10 for $\epsilon=-0.31$. Above and below the centerline of the worm one can see that it consists of a superposition of zig and zag convection rolls. These rolls are traveling towards the right; i.e., they enter the worm envelope on the left and leave it on the right. The envelope itself is moving only very slowly or not at all.

As ϵ increases to positive values, the cell fills entirely with convection. In the extended-chaos regime the pattern is a superposition of right- and left-traveling zig and zag rolls. A snapshot is shown in the bottom portion of Fig. 13. These patterns are very similar to those reported in Ref. [9]. At small σ in the worm regime, the patterns are somewhat more complicated, as shown in the top part of Fig. 13. The worm structures are still discernible and the spacing between them has become small; but in addition one has the impression of a superposition of extended structures consisting of zig and zag rolls.

IV. SUMMARY AND OUTLOOK

We showed that measurements of the critical behavior of thermally induced fluctuations can be used to estimate the critical voltage V_c of the conduction state. In the extended-chaos regime (relatively large conductivities) we found that the director-angle fluctuations $\langle\theta^2\rangle$ and the correlation length ξ have, within our experimental resolution, the ϵ dependence expected on the basis of mean-field theory and diverge at the same point where the amplitude of the flowfields above onset begins to grow. This is consistent with a supercritical bifurcation, as concluded previously [9].

For smaller conductivities, the measurements of V_c showed that the bifurcation from the conduction state to worms is subcritical. We determined the smallest voltage V_s at which worms formed at all, and defined $\tilde{\epsilon}_s=V_s^2/V_c^2-1$ as the range of the subcritical worm regime. We measured $\tilde{\epsilon}_s$ as a function of σ. Our data were not detailed enough to determine whether $\tilde{\epsilon}_s$ simply crossed the line $\epsilon=0$ at a finite angle or whether $\tilde{\epsilon}_s$ vanished in proportion to $(\sigma_c-\sigma)^2$ as expected for a tricritical bifurcation at σ_c. The former is expected on the basis of recent theoretical calculations by Treiber and Kramer [24], who found that the worm saddle node is not directly connected to the supercritical bifurcation to the extended state. The latter would be the more usual situation [31,32] when a subcritical bifurcation evolves into a supercritical bifurcation via a tricritical bifurcation.

The determinations of $\tilde{\epsilon}_s$ have been quite time consuming, and their σ resolution is limited by drifts in the conductivity of the samples. Nonetheless we feel that eventually it may be possible to obtain data with sufficient resolution to decide experimentally between the two cases considered above, namely, whether $\tilde{\epsilon}_s\propto\sigma-\sigma_c$ or whether $\tilde{\epsilon}_s\propto(\sigma-\sigma_c)^2$. Another way to determine the nature of the bifurcation near σ_c is to measure the initial slope S_1 of the ϵ dependence of the mean-square amplitude of the director angle

$$\langle\theta^2\rangle=S_1\epsilon \tag{10}$$

above onset. In the supercritical regime this slope should diverge at σ_c as $(\sigma-\sigma_c)^{-1}$ if the bifurcation is of the tricritical type, whereas the calculations based on the WEM [24] predict that this slope should remain finite. Either of these approaches is a significant undertaking, and in the end unfortunately may be limited by sample stability.

ACKNOWLEDGMENT

This work was supported by the National Science Foundation through Grant No. DMR94-19168.

[1] For a recent review, see, for instance, M. C. Cross and P. C. Hohenberg, Rev. Mod. Phys. **65**, 851 (1993).

[2] For a recent review of pattern formation in liquid crystals, see L. Kramer and W. Pesch, Annu. Rev. Fluid Mech. **27**, 515 (1995); W. Pesch and U. Behn, in *Evolution of Spontaneous Structures in Dissipative Continuous Systems*, edited by F. H. Busse and S. C. Müller, Lecture Notes in Physics Vol. M55 (Springer, New York, 1998).

[3] For a discussion of the properties of liquid crystals, see, for instance, P. G. de Gennes and J. Prost, *The Physics of Liquid Crystals* (Clarendon Press, Oxford, 1993); S. Chandrasekhar, *Liquid Crystals* (Cambridge University Press, London, 1992); L. M. Blinov and V. G. Chigrinov, *Electro-optic Effects in Liquid Crystal Materials* (Springer, New York, 1994).

[4] For a discussion of early experiments, see, for instance, I. Rehberg, B. L. Winkler, M. de la Torre Juárez, S. Rasenat, and W. Schöpf, Festkoerperprobleme **29**, 35 (1989).

[5] U. Finkenzeller, T. Geelhaar, G. Weber, and L. Pohl, Liq. Cryst. **5**, 313 (1989).

[6] M. Dennin, G. Ahlers, and D. S. Cannell, in *Spatio-Temporal Patterns*, edited by P. Palffy-Muhoray and P. Cladis, SFI Studies in the Science of Complexity, Proc. Vol. XXI (Addison-Wesley, Reading, MA, 1994).

[7] M. Dennin, D. S. Cannell, and G. Ahlers, Mol. Cryst. Liq. Cryst. Sci. Technol., Sect. A **261**, 337 (1995).

[8] M. Dennin, M. Treiber, L. Kramer, G. Ahlers, and D. S. Cannell, Phys. Rev. Lett. **76**, 319 (1996).

[9] M. Dennin, G. Ahlers, and D. S. Cannell, Science **272**, 388 (1996).

[10] M. Dennin, G. Ahlers, and D. S. Cannell, Phys. Rev. Lett. **77**, 2475 (1996).

[11] M. Dennin, D. S. Cannell, and G. Ahlers, Phys. Rev. E **57**, 638 (1998).
[12] E. Moses, J. Fineberg, and V. Steinberg, Phys. Rev. A **35**, 2757 (1987).
[13] R. Heinrichs, G. Ahlers, and D. S. Cannell, Phys. Rev. A **35**, 2761 (1987).
[14] O. Thual and S. Fauve, J. Phys. (France) **49**, 1829 (1988).
[15] H. Riecke, Phys. Rev. Lett. **68**, 301 (1992).
[16] K. Lerman, E. Bodenschatz, D. S. Cannell, and G. Ahlers, Phys. Rev. Lett. **70**, 3572 (1993).
[17] Two-dimensional pulses were found [18] in numerical studies of complex Ginzburg-Landau equations for a subcritical bifurcation and two modes.
[18] R. J. Deissler and H. R. Brand, Phys. Rev. A **44**, R3411 (1991).
[19] H. Riecke and G. D. Granzow, Phys. Rev. Lett. **81**, 333 (1998).
[20] M. Treiber and L. Kramer, Mol. Cryst. Liq. Cryst. Sci. Technol., Sect. A **261**, 2164 (1995).
[21] H. R. Brand, C. Fradkin, P. L. Finn, W. Pesch, and P. E. Cladis, Phys. Lett. A **235**, 508 (1997).
[22] J. B. Swift and P. C. Hohenberg, Phys. Rev. A **15**, 319 (1977).
[23] Y. Tu, Phys. Rev. E **56**, R3765 (1997).
[24] M. Treiber and L. Kramer, Phys. Rev. E **58**, 1973 (1998).
[25] U. Bisang and G. Ahlers, Phys. Rev. Lett. **80**, 3061 (1998).
[26] I. Rehberg, S. Rasenat, M. de la Torre-Juarez, W. Schöpf, F. Hörner, G. Ahlers, and H. R. Brand, Phys. Rev. Lett. **67**, 596 (1991).
[27] M. Dennin, Ph.D. thesis, University of California at Santa Barbara, 1995 (unpublished).
[28] S. Rasenat, G. Hartung, B. L. Winkler, and I. Rehberg, Exp. Fluids **7**, 412 (1989).
[29] For the isotropic Rayleigh-Bénard system, this method was discussed by M. Wu, G. Ahlers, and D. S. Cannell, Phys. Rev. Lett. **75**, 1743 (1995).
[30] For isotropic systems, the effect of external noise is discussed by P. C. Hohenberg and J. B. Swift, Phys. Rev. A **46**, 4773 (1992).
[31] A. Aitta, G. Ahlers, and D. S. Cannell, Phys. Rev. Lett. **54**, 673 (1985).
[32] L. Thomas, W. Pesch, and G. Ahlers, Phys. Rev. E **58**, 5885 (1998).